Effect of Micro-segregation on High Temperature Microstructure Evolution in Rapid Solidification Processed Nb-rich Ni-superalloys

Pablo D. Enrique *, Ali Keshavarzkermani, Norman Y. Zhou

*Corresponding author: pdenriqu@uwaterloo.ca, 519-888-4567 ext. 35625

Affiliation of P.D. Enrique, A. Keshavarzkermani, and Prof. N.Y. Zhou:
Department of Mechanical and Mechatronics Engineering, University of Waterloo
200 University Ave W, Waterloo, Ontario, N2L 3G1, Canada.

This is an author generated post-print of the article:

P.D. Enrique, A. Keshavarzkermani, N.Y. Zhou, Effect of micro-segregation on high temperature microstructure evolution in rapid solidification processed Nb-rich Ni-superalloys, Adv. Eng. Mater. (2021).

This manuscript version is made available under a CC-BY-NC-ND 4.0 license.
The final citeable publication can be found here: https://doi.org/10.1002/adem.202001396

Abstract

Rapid solidification processes are used for the coating, repairing, and manufacturing of metal alloy components in numerous industries. However, many alloys experience micro-segregation of elements at subgrain boundaries at the termination of solidification, which have potential consequences for phase transformations at elevated temperatures if used without homogenization heat treatments. Here, the effect of this micro-segregation and solidification microstructure on the coarsening kinetics of the δ phase in a Nb-rich Ni-superalloy is evaluated. Micro-segregation in rapid solidification processed alloy 718 results in a greater availability of nucleation sites for the precipitation of the δ phase, resulting in smaller precipitate sizes. Coarsening of the δ phase is found to follow a Lifshitz-Slyozov-Wagner model, which is used to determine that Nb diffusion is the limiting factor in δ phase coarsening. With the formation of the δ phase, and the concurrent coarsening and dissolution of the γ” strengthening phase, a decrease in both tensile strength and microhardness were observed. An improved understanding of the influence of micro-segregation on phase transformations allows for a more informed application of non-homogenized, rapid solidification processed alloys in industry.

Keywords: micro-segregation, solidification microstructure, subgrain, nucleation, coarsening, direct aging

---

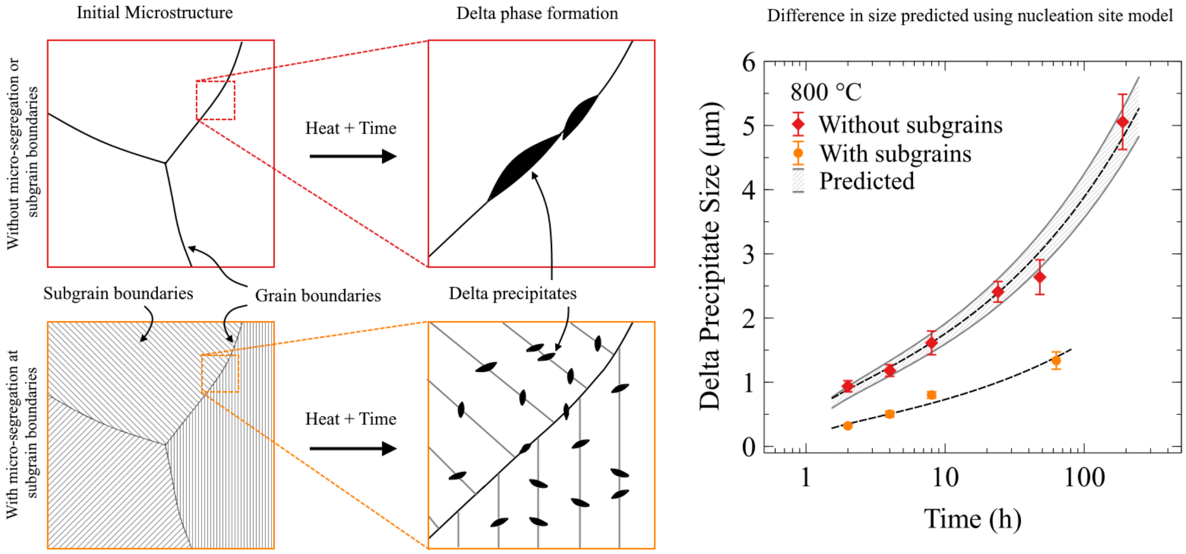

1. Introduction

Rapid solidification processing of metal alloys has been widely used for the application of coatings, the repair and joining of components, and the additive manufacturing of entire parts. Laser, electron beam, arc, and electrospark techniques fall under this classification, which are based on molten droplet transfer or self-quenching mechanisms [1]. The high cooling rates achieved by these mechanisms – through a combination of high temperature gradient and/or high solidification front velocity [2] – result in a finer subgrain microstructure which is expected to reduce but not eliminate micro-segregation of alloying elements [1]. Micro-segregation arises during solidification due to the solid phase's rejection of less soluble and slower diffusing elements into the liquid phase. At the terminus of solidification, the final liquid cools to form a eutectic or phases enriched in these elements. This non-equilibrium compositional variation between the core subgrains and subgrain boundary regions of an alloy can influence mechanical properties, microstructure evolution, and phase transformations during subsequent processing or use.

In some rapid solidification processed Ni-superalloys such as alloy 625 and alloy 718, the subgrain boundaries contain a Nb-rich eutectic and Nb-rich Laves phase. This Laves phase is widely reported as detrimental to mechanical properties, with low fracture toughness that facilitates crack propagation and reduces creep lifetime [3], tensile strength [4][5], and fatigue life at high stress amplitudes [6][7]. Although solution annealing heat treatments can be applied to homogenize the microstructure and redistribute micro-segregated elements, these alloys are frequently used in a direct aged condition where a strengthening phase is precipitated without first homogenizing the microstructure. Comparatively few studies have focused on the microstructural evolution and phase transformations resulting from compositional variation when these non-homogenized materials are exposed to elevated operating temperatures. Lass et al. have observed the growth of the δ phase (Ni_3Nb) along subgrain boundaries in laser powder bed fusion additive manufactured alloy 625 during the industry-recommended post-process heat treatment [8]. Similar observations were presented by Qi et al. [9] and Zhang et al. [10] for alloy 718, with a more in-depth study on the formation of the δ phase performed by Lyu et al. [11], who found that the precipitation rate of the δ phase in a rapid solidification processed (RSP) alloy 718 could be influenced by encouraging a more homogenized initial microstructure. These results can be attributed to partial dissolution of the Laves phase, which increases the amount of available Nb, and the low diffusion of Nb, which results in Nb-rich subgrain boundaries that encourage nucleation of the δ phase at elevated temperatures. A useful application of this phenomenon was presented by Liu et al. [12], which made use of the Laves to δ phase transformation to then homogenize alloy 718 with a lower temperature heat treatment. More recently, Huang et al. [13] constructed time-temperature-transformation diagrams for the various phases in laser additive manufactured alloy 718, finding notable differences when compared to the wrought material.

Exposure of alloys to elevated temperatures occurs frequently during standard heat treatments, transient overheating events during use [14][15], or even during the reheating of previous layers that occur in additive manufacturing processes [16], indicating that an improved understanding of the microstructural evolution is warranted. The methodology used here quantifies the effect of micro-segregation during rapid solidification processes on δ phase formation at elevated temperatures in Nb-rich Ni-superalloys, which can similarly be used to predict the size of secondary phases in other micro-segregated alloys after heat-treatment. As demonstrated in this study, the exposure of RSP alloy 718 to elevated temperatures results in the formation of δ precipitates at subgrain boundaries, whereas homogenized alloy 718 forms δ precipitates primarily along grain boundaries. An observed decrease in δ precipitate size and increase in the number of precipitates in RSP alloy 718 is well explained with the use of a nucleation site model, providing support for previous assumptions that the presence of Nb at subgrain boundaries is what encourages nucleation of the δ phase at those locations. An analysis of the δ phase coarsening kinetics suggest that the rate of Laves phase dissolution is not the limiting factor. Instead, the diffusion of Nb within the matrix is found to be the limiting factor for δ phase coarsening in rapid solidification processed Nb-rich Ni-superalloy.

2. Material and Methods

Rapid solidification processing is performed using electrospark deposition, which operates by discharging a capacitor to form a short duration spark that transfers material from an electrode (anode) to a substrate (cathode). Small droplets of electrode material (< 1 nL) splash onto the substrate surface and rapidly solidify. The small volume of transferred material, comparatively large substrate size which acts as a heat sink, and a typical 95 % cooling time between subsequent capacitor discharges result in an overall low heat input and very fast cooling rates up to 10^9 °C/s at the terminus of solidification [17]. Electrospark deposition was performed using a Huys Industries manual ESD machine at 90 V, 120 μF, and 170 Hz, with four passes performed in a raster scan pattern. A 5.0 grade ultra high purity argon shielding gas was delivered coaxially during deposition at a flow rate of 10 L/min.

For this study, an as-received alloy 718 substrate in the solution annealed condition (in accordance with SAE AMS5596 and ASTM B670 specifications) was coated with an alloy 718 electrode (3 mm diameter) using electrospark deposition. The composition of both materials is listed in Table 1. Each sample therefore contains both rapid solidification processed (RSP) alloy 718 and solution annealed (SA) alloy 718. This configuration allows for both material conditions to be heat treated and evaluated simultaneously. Since electrospark deposition results in a heat affected zone size of up to 80 μm for this material combination [18], care was taken to evaluate the substrate sufficiently far from the coating.

Table 1. EDX Composition (wt%) of alloy 718 electrode and substrate

Alloy 718	Ni	Cr	Fe	Nb	Mo	Ti	Al
Electrode	49.6	18.1	17.2	5.8	5.1	1.5	0.9
Substrate	50.1	17.2	17.4	5.9	4.1	1.4	1.0

The RSP alloy 718 and SA alloy 718 were aged with a two-step process to obtain a precipitation hardened state in which alloy 718 is more commonly used. The temperature was ramped to 720 °C at 5 °C/min in an argon environment and held for 8 hours, after which the samples were furnace cooled to 620 °C and held for 10 hours. At the conclusion of the holding period, the samples were removed from the furnace and allowed to air cool. These two material conditions, rapid solidification processed and aged (RSP + aged) and solution annealed and aged (SA + aged) are then subjected to elevated temperatures of 700 °C, 800 °C, and 900 °C for various durations to determine the effect of micro-segregation on phase transformations. These heat treatments were performed in an air environment to simulate typical usage.

Sample cross-sections were etched with inverted glyceregia composed of HCl:HNO3:Glycerol in a 5:1:1 ratio for up to 2 minutes depending on the extent of heat treatment, and images of the microstructure were obtained using a Zeiss UltraPlus scanning electron microscope (SEM). Measurements of the δ phase long axis were made using ImageJ software, and MATLAB was used to obtain best fit curves for the experimental data. A JEOL7000F SEM with an Oxford electron backscatter diffraction (EBSD) detector was used for determination of grain boundary misorientation, and a MicroLab 350 Auger Microprobe is used for obtaining the composition of small phases using Auger electron spectroscopy (AES). Tensile testing was performed on an Instron 5548 micro tensile tester at 1 mm/min, using non-standard tensile specimens as shown in Figure 1. The small specimen sizes were designed to accommodate the small deposition volumes and long deposition times associated with high-quality ESD repairs. ESD process parameters were kept the same at those used for the microstructure analysis, and the specimens were created using a double U-joint repair in which one cavity was created and repaired at a time. The two notches were created using a Struers Accutom-50 precision saw and water cooling, to avoid microstructural changes from heat input during cutting. Microhardness measurements were performed on a Wolpert Wilson 402 MVD micro Vickers hardness tester using 100 gf and a 15 s dwell time.

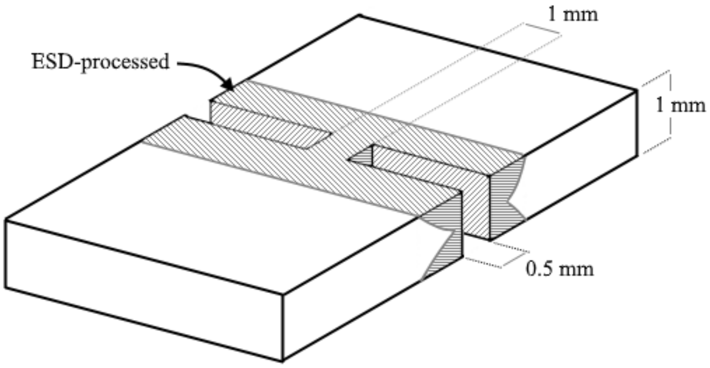

Figure 1. Specimen used for tensile testing with ESD repaired U-grooves

3. Results and Discussion

3.1 Microstructure Evolution

The rapid solidification processed (RSP) alloy 718 is primarily composed of low angle (2°) boundaries (Figure 2 area a), indicative of a slight misorientation between adjacent subgrains that form during solidification. The subgrain size is strongly dependent on the cooling rate, with a measured primary cell spacing ranging from 0.4 to 1.5 μm indicating that very high cooling rates are present [19]. The morphology of the subgrain is determined by the ratio of the temperature gradient *G* at the solid/liquid interface to the solidification rate (interface velocity) *R*. The obtained cellular or cellular dendritic morphology is indicative of a *G*/*R* ratio too large to fully form secondary dendrite arms. After an aging heat treatment is applied, the RSP + aged alloy 718 retains its subgrain microstructure (Figure 3a compared to Figure 3b) that includes the interdendritic eutectic and Laves phases at the subgrain boundaries. No notable change in grain or subgrain size is observed, however the aging process does result in the precipitation of carbides, as well as γ" (Ni_3Nb), and γ' ($Ni_3(Al,Ti)$) strengthening phases within the cellular subgrains (Figure 3b).

In contrast to the RSP alloy 718, the solution annealed (SA) alloy 718 contains equiaxed grains almost completely composed of high angle (60°) grain boundaries (Figure 2 area b). The lack of low angle solidification subgrain boundaries is indicative of recrystallization having occurred. After an aging heat treatment, the SA + aged alloy 718 forms carbides, γ", and γ' phases within the grain boundaries (Figure 3b). This aging heat treatment results in optimal strength and mechanical properties, arising from a γ" precipitate size of approximately 20 to 30 nm.

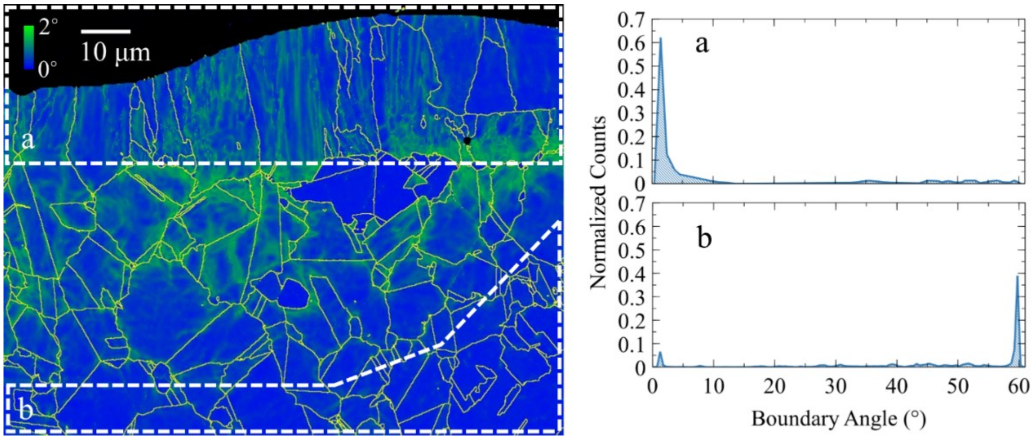

Figure 2. EBSD kernel average misorientation map of an alloy 718 a) coating and b) substrate with a respective count of grain boundary angle.

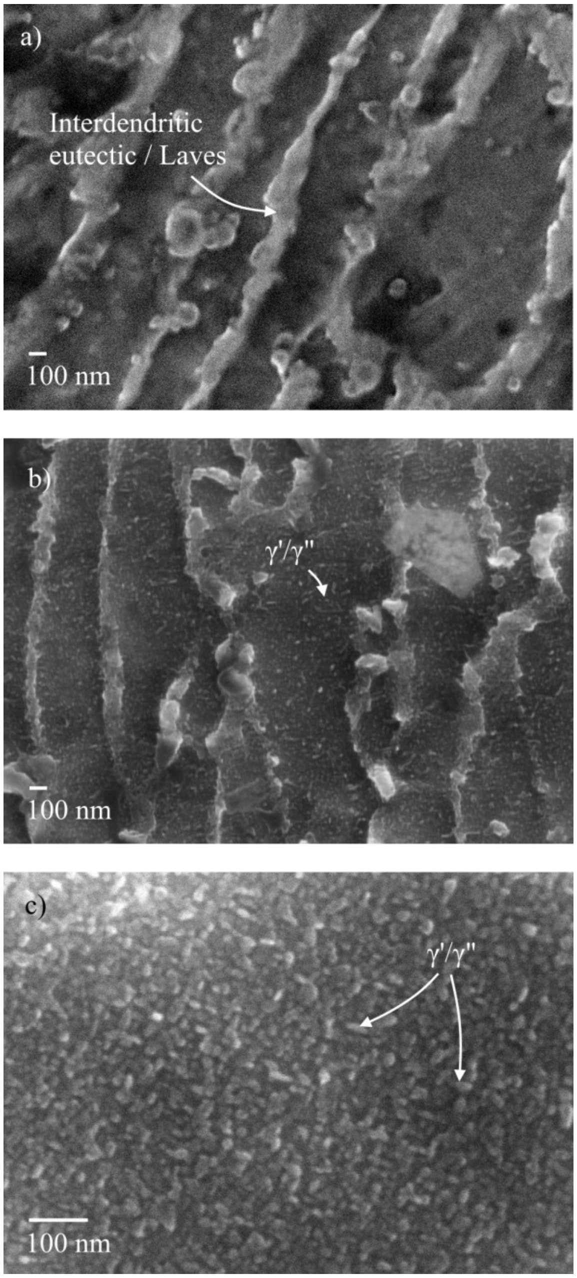

Figure 3. SEM images of the microstructure in a) RSP alloy 718, b) RSP + aged alloy 718, and c) SA + aged alloy 718

Exposure of the RSP + aged alloy 718 and SA + aged alloy 718 to elevated temperatures and longer durations results in significant microstructure evolution. RSP + aged alloy 718 forms the δ phase at the interdendritic eutectic along the subgrain boundaries, as shown in Figure 4a. AES results in Figure 4d show the clear presence of Nb and Ni peaks at these locations. The presence of C and O peaks are due to contamination and oxidation on the sample surface, and their high peaks can be attributed to the high surface sensitivity of AES. Higher magnification images (Figure 4b) show that precipitation of the γ” phase with Ni_3Nb composition - identifiable due to its elliptical cross-sections and the presence of Nb and Ni Auger peaks in Figure 4f - also occurs preferentially near the Nb-enriched subgrain boundaries. However, the spherical γ’ phase forms throughout the γ matrix, since its $Ni_3(Al,Ti)$ composition is not influenced by Nb micro-segregation at the subgrain boundaries. AES spectra of these spherical phases show clear Ti and Ni peaks (Figure 4c), and analysis of the γ matrix in the core dendrite region also shows a sharp Ti peak, alongside the expected Cr, Fe and Ni peaks (Figure 4e).

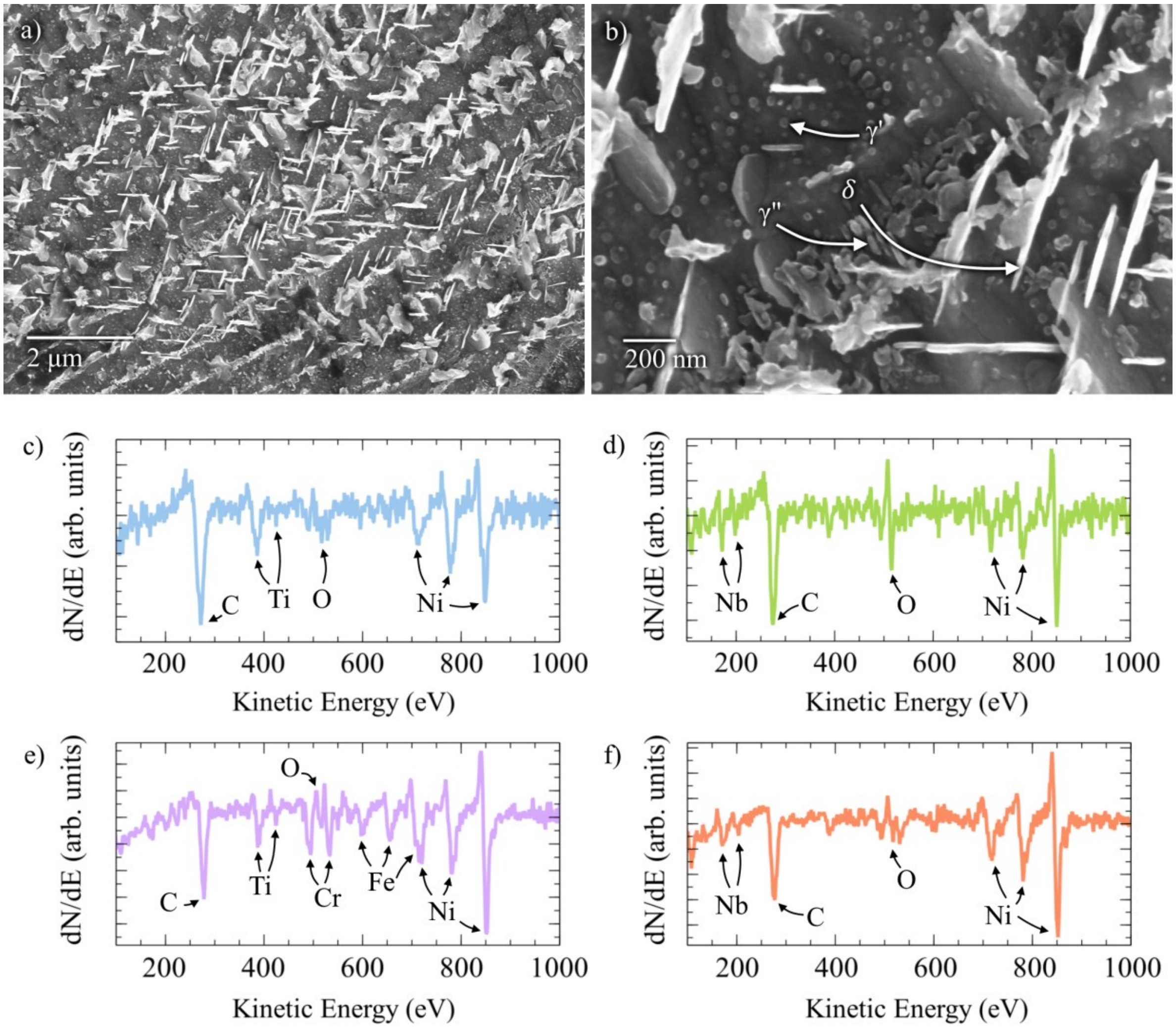

Figure 4. SEM images of the etched microstructure in a) RSP + aged alloy 718 exposed to 800 °C for 4 h, b) higher magnification image of the interdendritic region, AES derivative spectrum of c) γ’ phase, d) δ phase, e) γ matrix in the dendrite core, and f) γ” phase

Similar microstructure evolution is observed in RSP + aged alloy 718 at 700 °C (Figure 5a), 800 °C (Figure 5b), and 900 °C (Figure 5c), although with differing times required before the δ phase is observed. The microstructure in Figure 5 shows differences in subgrain growth directions between adjacent grains in the RSP + aged alloy 718. This difference can be attributed to the substrate grain orientation, a small portion of which is shown in the images in Figure 5. During solidification, the heterogeneous nucleation of grains on the substrate is expected to be more favourable than the growth of new grains via heterogeneous nucleation. As such, the nucleated grains adopt the crystallographic orientation of the grains in the substrate and the subgrains that form can appear tilted when viewed along the cross-section.

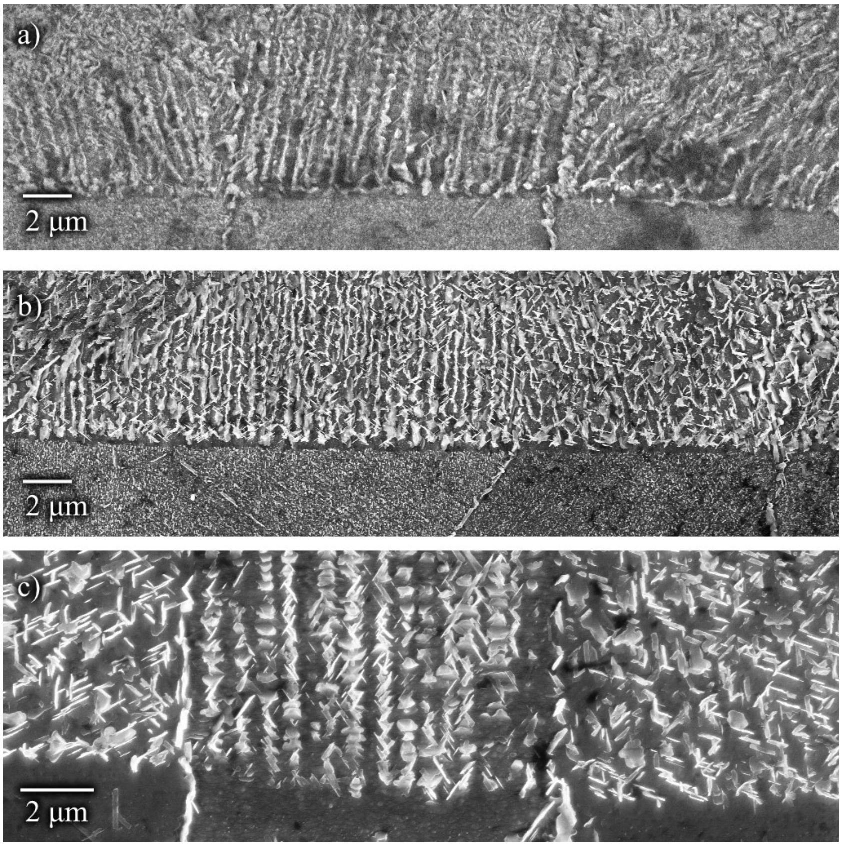

Figure 5. SEM images of the etched microstructure in RSP + aged alloy 718 after exposure to a) 700 °C for 100 h, b) 800 °C for 2 h, and c) 900 °C for 0.5 h. A portion of the substrate is visible at the bottom of each image.

In SA + aged alloy 718, the γ” phase also experiences coarsening while the δ precipitates grow at the grain boundaries (Figure 6a). The formation of a γ” depletion region surrounding the δ phase

(Figure 6b) suggests that formation of δ precipitates occurs alongside the dissolution of γ”, and contrasts sharply with the RSP + aged alloy 718 which showed a clustering of both γ” and δ precipitates at the subgrain boundaries (Figure 4b). Alongside coarsening of the γ” phase, a change in the γ” morphology from a rounded, short disc shape to a more elongated shape with sharper features is observed. Similar changes in morphology have been previously observed in the literature for over-aged γ” particles in alloy 718 [20]–[22] and other similar alloys [23].

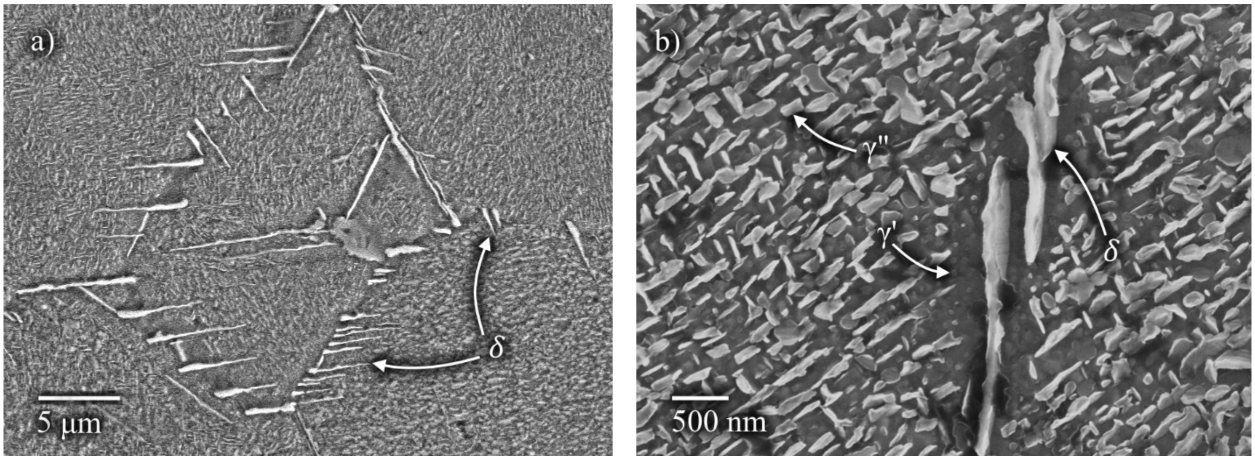

Figure 6. SEM images of the etched microstructure in a) SA + aged alloy 718 exposed to 800 °C for 24 h and b) higher magnification image showing δ phase with adjacent region depleted of γ”

3.2 Formation of the δ phase

The formation of a new phase occurs in three stages: nucleation, growth, and coarsening. Nucleation occurs when a cluster of atoms forms a thermodynamically stable nuclei larger than the critical radius, which is a function of the change in volume Gibbs free energy and interfacial energy [24]. The presence of compositional variations due to micro-segregation is expected to facilitate the formation of nuclei at subgrain boundaries for the δ phase in alloy 718. Once the critical radius is surpassed, growth of the precipitate occurs via the attachment of atoms diffusing from the surrounding solid solution. As growth progresses, coarsening begins to occur via the dissolution of smaller precipitates. The number of sites at which nucleation occurs therefore governs the number of precipitates that form and, along with the coarsening rate, governs the precipitate size. These aspects can be used to explain the disparity in δ precipitate microstructure between RSP + aged and SA + aged alloy 718.

Heterogeneous nucleation of new phases can preferentially occur at boundaries due to higher interfacial energy than in the bulk, as well as the availability of elements required for the nucleating phase [25]. In the case of RSP + aged alloy 718, Nb is available at subgrain boundaries due to micro-segregation during solidification. SA + aged alloy 718 has been shown to experience grain boundary segregation and precipitation [26][27] when exposed to elevated temperatures. To quantify the number of potential nucleation sites at grain and subgrain boundaries, a nucleation site model is applied. Grains and subgrains are approximated as adjacent tetrakaidecahedrons, with surfaces, edges, and corners considered sites that favor nucleation. The number of grain/subgrain surface (N_s), edge (N_e) and corner nucleation sites (N_c) are expressed in Equations 1 to 3, respectively. These equations are constructed by taking expressions for surface area, edge length, or corner sites in one embedded tetrakaidecahedron as shown by Rajek [28] and extended to a volume of 1 m^3.

$$N_s = \frac{6\left(1+2\sqrt{3}\right)\lambda^2 + 2\lambda(2H+\lambda)}{16\sqrt{2}\lambda^3 + 12\lambda^2 H}\left(\frac{N_A}{V_m}\right)^{\frac{2}{3}} \tag{1}$$

$$N_e = \frac{36\lambda + 8H}{24\sqrt{2}\lambda^3 + 18\lambda^2 H}\left(\frac{N_A}{V_m}\right)^{\frac{1}{3}} \tag{2}$$

$$N_c = \frac{6}{8\sqrt{2}\lambda^3 + 6\lambda^2 H} \tag{3}$$

where N_A is Avogadro's number, V_m is the molar volume of Ni (6.6×10^6 m^{3}mol^{-1}), λ is dependent on the grain/subgrain diameter (d) as shown in Equation 4, and H is dependent on the grain/subgrain diameter and length (D) as shown in Equation 5.

$$\lambda = \frac{d}{\sqrt{10}} \tag{4}$$

$$H = \sqrt{\left(D^2 - \frac{d^2}{5}\right)} - 2\sqrt{\frac{d^2}{5}} \tag{5}$$

The use of diameter and length values representative of the microstructure visible in Figure 2 and Figure 3a result in a 3.5 times increase in available nucleation sites within the RSP + aged alloy 718 when compared to the SA + aged alloy 718 (Table 2). The corresponding difference in precipitate size can be evaluated by considering the thin disk-like shape of the δ phase [29] and a 3.5 times difference in volume as a result of the difference in nucleation sites. Assuming the precipitate size is scaled proportionately along the thickness and diameter dimensions, the following expression can be used to relate the volumes of δ precipitates in the RSP + aged alloy 718 (V_{RSP}) and SA + aged alloy 718 (V_{SA}):

$$V_{SA} = 3.5V_{RSP} = 2.4l_{RSP}\pi\left(\frac{2.4d_{RSP}}{2}\right)^2 \qquad (6)$$

where the diameter (d_{RSP}) and thickness (l_{RSP}) of a δ precipitate in the RSP + aged alloy 718 (with the subgrain boundaries) are expected to be smaller by a factor of 2.4 when compared to a δ precipitate in the SA + aged alloy 718 (without subgrains boundaries). Although the difference in the number of nucleation sites are used to establish a relationship between the δ precipitate sizes in the two alloy 718 conditions, the actual δ precipitate sizes are also a function of the coarsening rate, which is influenced by the heat treatment time and temperature.

Table 2. Nucleation sites in an RSP + aged alloy 718 and SA + aged alloy 718 using a tetrakaidecahedron model

	RSP + aged		**SA + aged**
	Subgrain	**Grain**	**Grain**
d [m]	5.0×10^{-7}	7.6×10^{-6}	5.7×10^{-6}
D [m]	2.0×10^{-5}	2.1×10^{-5}	5.7×10^{-6}
N_s [m^{-3}]	4.5×10^{25}	4.9×10^{24}	1.4×10^{25}
N_e [m^{-3}]	8.2×10^{22}	4.7×10^{20}	1.5×10^{21}
N_c [m^{-3}]	2.0×10^{18}	9.9×10^{15}	9.1×10^{16}
Total sites [m^{-3}]	5.0×10^{25}		1.4×10^{25}

The coarsening of δ precipitates in RSP + aged and SA + aged alloy 718 is expected to follow the Lifshitz-Slyozov-Wagner theory of Ostwald ripening for volume diffusion-controlled coarsening. This has previously been used to model the growth of γ” precipitates [30][31], with modifications made to account for the disc-shaped particle morphology [32]. These same modifications can be used for the disc-shaped δ phase, such that the coarsening of the δ particles follows:

$$d^3 = kt + d_0^3 \qquad (7)$$

where t is the time, d is the particle diameter, d_0 is the initial particle diameter at $t = 0$, and k is a combination of the diffusion coefficient (D), temperature (T), precipitate interfacial energy (γ), equilibrium concentration of the solute species (c_0), precipitate volume (V_m), particle aspect ratio (K), and the ideal gas constant (R) as shown in Equation 8. The diffusion coefficient can be further expanded into Equation 9, which is shown to depend on the activation energy (E_a) and temperature.

$$k = \frac{128}{9\pi}\frac{\gamma K c_0 V_m^2 D}{RT} \qquad (8)$$

$$D = D_0 \exp\left(\frac{-E_a}{RT}\right) \qquad (9)$$

Equation 7 is used to produce best fit curves for experimental measurements of δ precipitate size in RSP + aged and SA + aged alloy 718 after exposure to 800 °C, shown as the dashed lines in Figure 8Figure 7. Equation 6 is used to generate a prediction of the δ precipitate size in SA + aged alloy 718 based on the measured sizes (orange circles) in RSP + aged alloy 718. The 99% confidence interval for this prediction is shown in Figure 7 as the grey shaded region and an excellent match between the predicted and measured precipitate size for SA + aged alloy 718 (in red) is obtained. This suggests that the difference in precipitate size between RSP + aged and SA + aged alloy 718 is accurately explained by the increase in nucleation sites made available due to micro-segregation that occurs at subgrain boundaries during solidification, and the change in precipitate size over time follows a Lifshitz-Slyozov-Wagner model.

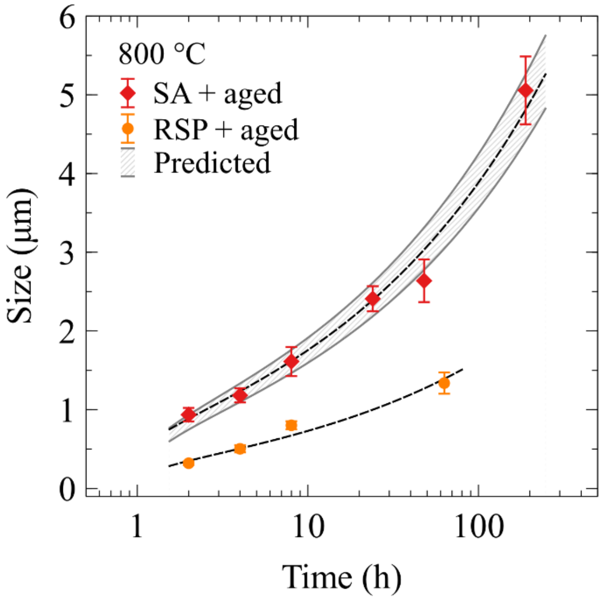

Figure 7. a) Growth of δ phase in RSP + aged and SA + aged alloy 718

Experimental measurements of the δ particle diameters at three temperatures in the RSP + aged alloy 718 are shown in Figure 8a. Equation 7 is used to apply a best fit curve to the measured data at each of the studied temperatures and the fit parameters are reported in Table 3. The value of k – which indicates how strongly the heat treatment affects the precipitate size – increases by two orders of magnitude within the temperature range investigated. This is explained by the strong temperature dependence of the diffusion coefficient (D), as shown in Equation 9, and suggests that the coarsening mechanism of the δ phase along the subgrain boundaries is limited by diffusion. When exposed to 700 °C and 800 °C, the δ phase was not observed until 100 h and 2 h respectively. Samples in which no δ precipitates were observed are marked in Figure 8a as having a 0 µm size.

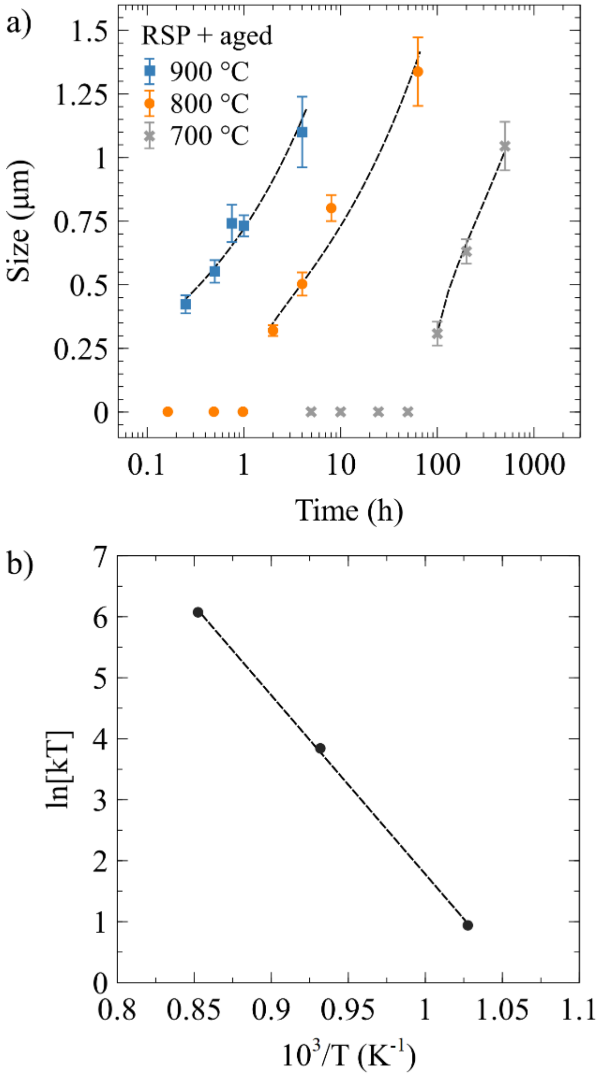

Figure 8. a) Size of the δ phase in RSP + aged alloy 718, b) an Arrhenius plot derived from the δ size measurements in (a)

Table 3. Model parameters for Equation 7 obtained from Figure 8a and the R-squared (R^2) statistic for model fit

Temperature (°C)	$\boldsymbol{k}$ **(μm² h⁻¹)**	$\boldsymbol{d_0}$ **(μm)**	$\boldsymbol{R^2}$
700	0.0026	-0.62	0.99
800	0.043	-0.35	0.97
900	0.38	-0.20	0.96

A further understanding of the δ phase coarsening mechanism can be obtained by determining the activation energy for diffusion. The expression resulting from the substitution of Equation 9 into Equation 8 can be rearranged into an Arrhenius form as shown in Equation 10, under the assumption that γ, K, c_0, V_m and D_0 are independent of temperature. The value of $\ln(kT)$ can then be plotted (Figure 8b) against $1/T$ using the values in Table 3, and the activation energy (E_a) can be determined from the slope of the best fit line. This activation energy for δ coarsening (244 kJ mol^{-1}) compares favorably to the activation energy for Nb diffusion in a Ni-superalloy (237 kJ mol^{-1} [33]), suggesting that Nb diffusion through the matrix is the limiting factor for δ phase coarsening in RSP alloy 718 with micro-segregation at the subgrain boundaries, rather than the dissolution of the Laves phase (275 kJ mol^{-1} [34]). One might expect that Laves dissolution would be rate limiting, since the activation energy for Laves dissolution is greater than that of Nb diffusion. However, if sufficiently large sources of solutionized Nb are available in the Ni matrix, the comparatively slow dissolution of the Laves phase would be of lesser consequence. Due to the formation of a Nb-rich interdendritic eutectic at the subgrain boundaries, this is likely the case in RSP alloy 718.

$$\ln(kT) = -\frac{E_a}{R}\frac{1}{T} + \ln\left(\frac{128}{9\pi}\frac{\gamma K c_0 V_m^2 D_0}{R}\right) \qquad (10)$$

3.3 Effect of the δ phase on mechanical properties

A comparison of RSP + aged alloy 718 after 0 h, 4 h, and 70 h of exposure to 800 °C shows an initial degradation in mechanical properties between 0 h and 4 h, and a less significant change afterwards (Figure 9). Both ultimate tensile strength (UTS) and microhardness experienced a decrease of 15% and 21%, respectively, after 70 h of heat treatment. The observed trend is broadly comparable to results previously reported in literature for alloy 718 [21], which observe a rapid initial drop and a more gradual decline afterwards.

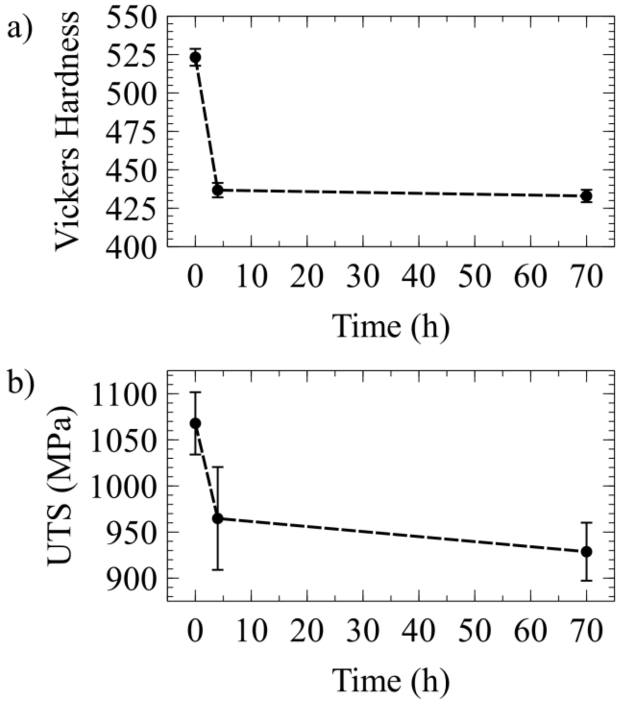

Figure 9. The influence of exposure time at 800 °C for a RSP+aged alloy 718 on a) microhardness and b) ultimate tensile strength (UTS)

All samples had sharp features on the fracture surface (Figure 10a), with dendritic features visible at higher magnification (Figure 10b), suggesting that plastic deformation is limited. As was shown previously in RSP [5] and RSP+aged [18] alloy 718, the crack propagation pathway continues to occur along subgrain and droplet boundaries according to the relative fracture toughness [5] even after the formation of the δ phase. However, in samples heat treated for 4h and 70h, many instances of secondary crack propagation show unbroken δ precipitates bridging the crack path (Figure 10c), as well as δ precipitates protruding from the primary fracture surfaces (Figure 10d). As a result, crack propagation does appear to be influenced by the presence of δ precipitates. Crack initiation was found to occur from the part surface or from Al- and Ti-rich oxide defects (Figure 10e) regardless of heat treatment time.

The crack propagation mechanism appears to switch from the typical particle cracking mode reported when only the Laves phase is present to a combination of micro void formation and interface debonding [35]. In addition to differences in properties between the δ and Laves phase, the orientation and growth of the δ phase into the γ matrix may introduce increased resistance to crack propagation by increasing the crack path tortuosity and slowing crack propagation occurring at lower stress levels. This has been shown in direct aged alloy 718 to have a notable influence on fatigue and creep properties [36], with a greater amount of δ phase particles more effectively reducing the crack propagation rate. For RSP+aged alloy 718, the use of longer heat treatments that produce δ precipitates > 1 µm in size are expected to be more effective at increasing crack propagation resistance, based on studies from other materials with grain boundary precipitates [35]. In combination with the dissolution of the brittle Laves phases, this would be expected to improve mechanical properties. However, these potential positive mechanisms occur alongside negative effects such as the coarsening of the γ” phase – the primary strengthening phase in alloy 718 – and the transformation of γ” into δ [21]. Previous studies have shown that a proper balance can be achieved between the reduced strength from dissolution of the γ” phase and formation of the δ phase, such that strength requirements are still met for most applications while significantly improving fatigue and creep properties [36].

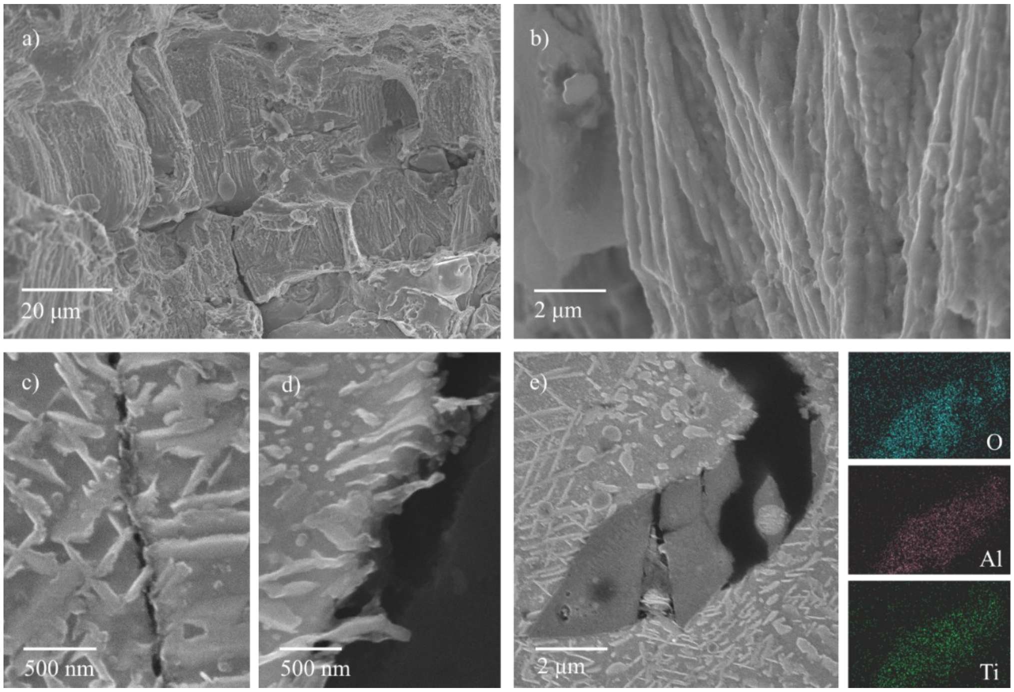

Figure 10. SEM images from tensile specimens exposed to 800 °C for 70 h showing a) fracture surface, b) high magnification of fracture surface showing dendritic features, cross-sections of fractured surface showing c) secondary crack pathway and d) crack pathway along primary fracture surface, and e) site of crack initiation with EDX maps for O, Al, and Ti

Conclusions

Micro-segregation at subgrain boundaries affects the precipitation of the δ phase in rapid solidification processed and aged (RSP + aged) alloy 718 by providing a greater number of nucleation sites, which results in a greater number of proportionally smaller δ precipitates than in a solution annealed and aged (SA + aged) alloy 718 without micro-segregation or subgrain boundaries. The coarsening of δ precipitates in RSP + aged alloy 718 follows a Lifshitz-Slyozov-Wagner model and the activation energy for coarsening matches that of Nb diffusion, suggesting that Laves or γ” dissolution is not the limiting factor.

The methodology used in this study establishes a clear relationship between the nucleation site density and the secondary phase size in rapid solidification processed alloys with critical alloying elements found at the subgrain boundaries. This influences not only the precipitate size, but also the distribution, which can be expected to influence mechanical properties. In the present study, the formation of fine subgrain boundary δ phase precipitates in RSP + aged alloy 718 is found to negatively influence hardness and ultimate tensile strength. Although δ precipitates appear to positively influence the crack propagation pathway during tensile fracture, the observed decrease in mechanical properties is primarily attributed to coarsening and transformation of the γ” strengthening phase that occurs alongside δ phase coarsening. This highlights the importance of understanding the microstructure evolution in micro-segregated alloys, which can allow for the prediction and control of precipitate size, precipitate distribution, and mechanical properties.

Acknowledgements

This work was performed with funding support from the Natural Sciences and Engineering Research Council of Canada (NSERC), the Canada Research Chairs (CRC) Program, Huys Industries, and the CWB Welding Foundation, in collaboration with the Centre for Advanced Materials Joining and the Multi-Scale Additive Manufacturing Lab at the University of Waterloo.

References

[1] E.J. Lavernia, T.S. Srivatsan, *J. Mater. Sci.* **2010**, *45*, 287.
[2] S. Kou, *Welding Metallurgy*, John Wiley & Sons, Inc., New Jersey, USA **2003**.
[3] L.Y. Wang, Z.J. Zhou, C.P. Li, G.F. Chen, G.P. Zhang, *Mater. Sci. Eng. A* **2019**, *745*, 31.
[4] A. Hilaire, E. Andrieu, X. Wu, *Addit. Manuf.* **2019**, *26*, 147.

[5] P.D. Enrique, Z. Jiao, N.Y. Zhou, E. Toyserkani, *Mater. Sci. Eng. A* **2018**, *729*, 268.

[6] S. Sui, J. Chen, E. Fan, H. Yang, X. Lin, W. Huang, *Mater. Sci. Eng. A* **2017**, *695*, 6.

[7] H.Y. Wan, Z.J. Zhou, C.P. Li, G.F. Chen, G.P. Zhang, *Adv. Eng. Mater.* **2018**, *20*, 1.

[8] E.A. Lass, M.R. Stoudt, M.E. Williams, M.B. Katz, L.E. Levine, T.Q. Phan, T.H. Gnaeupel-Herold, D.S. Ng, *Metall. Mater. Trans. A Phys. Metall. Mater. Sci.* **2017**, *48*, 5547.

[9] H. Qi, M. Azer, A. Ritter, *Metall. Mater. Trans. A Phys. Metall. Mater. Sci.* **2009**, *40*, 2410.

[10] D. Zhang, W. Niu, X. Cao, Z. Liu, *Mater. Sci. Eng. A* **2015**, *644*, 32.

[11] F. Lyu, F. Liu, X. Hu, X. Yang, C. Huang, D. Shi, *Materials (Basel).* **2019**, *12*.

[12] F. Liu, F. Lyu, F. Liu, X. Lin, C. Huang, *J. Mater. Res. Technol.* **2020**, *9*, 9753.

[13] W. Huang, Z. Wang, *Adv. Eng. Mater.* **2020**, *2000982*, 1.

[14] J. Lu, Z. Yang, Y. Zhou, J. Huang, J. Yan, Y. Dang, Y. Yuan, Y. Gu, *Eng. Fail. Anal.* **2019**, *97*, 227.

[15] R.E. Dundas, in *Vol. 2 Combust. Fuels; Oil Gas Appl. Cycle Innov. Heat Transf. Electr. Power; Ind. Cogener. Ceram. Struct. Dyn. Control. Diagnostics Instrumentation; IGTI Sch. Award*, American Society Of Mechanical Engineers**1993**, V002T10A003.

[16] C. Kumara, A. Segerstark, F. Hanning, N. Dixit, S. Joshi, J. Moverare, P. Nylén, *Addit. Manuf.* **2019**, *25*, 357.

[17] J. Gould, *Weld. J.* **2011**, *90*, 191.

[18] P.D. Enrique, Z. Jiao, N.Y. Zhou, *Metall. Mater. Trans. A* **2019**, *50*, 285.

[19] P.D. Enrique, Z. Jiao, N.Y. Zhou, E. Toyserkani, *J. Mater. Process. Technol.* **2018**, *258*, 138.

[20] J. Dong, X. Xie, Z. Xu, S. Zhang, M. Chen, **2012**, 649.

[21] M. Jouiad, E. Marin, R.S. Devarapalli, J. Cormier, F. Ravaux, C. Le Gall, J.M. Franchet, *Mater. Des.* **2016**, *102*, 284.

[22] C. Slama, C. Servant, G. Cizeron, *J. Mater. Res.* **1997**, *12*, 2298.

[23] L.M. Suave, D. Bertheau, J. Cormier, P. Villechaise, A. Soula, Z. Hervier, J. Laigo, *MATEC Web Conf.* **2014**, *14*, 21001.

[24] L. Ratke, P.W. Voorhees, in *Growth and Coarsening*, **2002**, 205.

[25] M. Gao, R.P. Wei, *Scr. Metall. Mater.* **1995**, *32*, 987.

[26] X.J. Pang, D.J. Dwyer, M. Gao, P. Valerio, R.P. Wei, *Scr. Metall. Mater.* **1994**, *31*, 345.

[27] D.H. Ping, Y.F. Gu, C.Y. Cui, H. Harada, *Mater. Sci. Eng. A* **2007**, *456*, 99.

[28] H. Rajek, *Computer Simulation of Precipitation Kinetics in Solid Metals and Application to the Complex Power Plant Steel CB8*, Graz University of Technology, **2005**.

[29] J. Lacaze, M. Dehmas, A. Niang, B. Viguier, *Adv. Mater. Sci. Eng.* **2011**, *2011*.

[30] C. Zhang, L. Yu, H. Wang, *Materials (Basel).* **2019**, *12*, 2096.

[31] A. Devaux, L. Nazé, R. Molins, A. Pineau, A. Organista, J.Y. Guédou, J.F. Uginet, P. Héritier, *Mater. Sci. Eng. A* **2008**, *486*, 117.

[32] J.D.J. Boyd, R.. B. Nicholson, *Acta Metall.* **1971**, *19*, 1379.

[33] M.J. Sohrabi, H. Mirzadeh, *Met. Mater. Int.* **2019**.

[34] M. Rafiei, H. Mirzadeh, M. Malekan, M.J. Sohrabi, *J. Alloys Compd.* **2019**, *793*, 277.

[35] S. Kumar, W.A. Curtin, *Mater. Today* **2007**, *10*, 34.

[36] S. Li, J. Yang, J. Zhuang, Q. Deng, J. Du, X. Xie, B. Li, Z. Xu, Z. Cao, Z. Su, C. Jiang, **2012**, 545.